Influence of specimen width on the elongation to fracture in cyclic bending under tension of commercially pure titanium sheets

Talukder Musfika Tasnim Oishi[a], Nick Pitkin[a], Nathan Miller[b], Desmond Mensah[a], David T. Fullwood[b], Michael P. Miles[c], Brad L. Kinsey[a], and Marko Knezevic[a,*]

[a] Department of Mechanical Engineering, University of New Hampshire, Durham, NH 03824.
[b] Department of Mechanical Engineering, Brigham Young University, Provo, UT 84602
[c] Department of Manufacturing Engineering, Brigham Young University, Provo, UT 84602

[*] Corresponding author e-*mail address*: marko.knezevic@unh.edu (M. Knezevic).

Abstract

In recent publications, we have shown that repeated bending and unbending during tension can significantly increase the percent elongation to failure (ETF) of metallic sheets. A custom-built machine for cyclic bending under tension (CBT) testing was designed and used to test several sheet metals. In particular, the improvements in ETF using CBT were over 3× relative to simple tension (ST) for commercially pure titanium (cp-Ti) sheets. The present paper evaluates the influence of specimen width on the achieved ETF in CBT of cp-Ti sheets. To facilitate the study, the CBT machine was furnished with wide grips to enable processing of sheets in addition to testing narrow strips. The ETF was observed to reduce with the sheet width. To rationalize the observations, the strain rate-independent plasticity theory of von Mises (J_2) with isotropic expansion of yield surfaces of cp-Ti was used in finite elements (FE) to perform a set of simulations. To facilitate the FE simulations of the CBT process stretching the sheets of cp-Ti far beyond the point of maximum uniform strain in ST, the post-necking hardening behavior was inferred along RD, TD, and 45 sheet directions using an established methodology combining ST tests, CBT tests, and modeling material behavior during CBT. Simulated geometries and mechanical fields were found to be in good agreement with corresponding measurements for every specimen width. While predicted axial strains were similar for every width, the strain path shifted from uniaxial tension for the narrow specimen toward plane-strain tension for the wider specimens. As such, as plane-strain tension was approached via progressively wider specimens, the width strain was reduced, while the thinning strains increased. The increase in the thinning strain was established as the primary reason for the reduced ETF with increasing sheet width. Experimental and FE simulation results along with the insights into the influence of specimen width on the ETF in CBT of cp-Ti are presented and discussed.

Keywords: Elongation-to-fracture; Strain hardening; Cyclic-bending-under-tension; Commercially purity titanium; Specimen width

1. Introduction

Tradeoffs in strength and ductility of metallic sheets are usually achieved by alloy design and innovative processing involving heat treatment and deformation operations. Additionally, sheets can be formed using strain path planning, such that greater elongation-to-failure (ETF) is achieved. The non-conventional cyclic bending under tension (CBT) is one such process, which delays localized necking to achieve significantly greater strain levels than those obtained in simple tension (ST) [1, 2]. Owing to the large plastic strains imparted by CBT, and underlying microstructural evolution, high strength [3] and increased R-value [4] can be realized in the processed sheets. Delaying localized necking is particularly important for hexagonal close-packed (HCP) materials, such as Mg and Ti alloys, which suffer from limited ductility but have many desirable intrinsic properties, e.g., low mass and high strength [5]. Poor formability of HCP metals at room temperature is associated with difficulties to activate enough slip systems on basal, prismatic, and pyramidal slip planes and the need for deformation via twinning [6-11]. Nevertheless, HCP metals are being increasingly evaluated for structural components owing to their high strength-to-weight ratio. In particular, the use of Ti and its alloys in the manufacture of parts and machine components has increased greatly owing to ease of fabrication, excellent corrosion resistance, and relatively high strength-to-weight ratio. Examples include dental and orthopedic implants in the medical field [12], airframe and engine components in aerospace manufacturing [13-15], forced-induction and suspension components in automotive manufacturing [16], among many other applications. Commercially pure titanium (cp-Ti) sheets exhibit some anisotropy in their deformation behavior and have modest ductility at room temperature [17, 18] and strain rate sensitivity [19-21]. The sheets can be formed at room temperature by press forming but usually elevated temperatures are required to achieve the desired part shape (via superplastic forming) [22, 23]. The plasticity of cp-Ti is accommodated by crystallographic slip along with some twinning, depending on the grade [24-26].

The underlying mechanisms for the CBT process to improve ETF pertain to suppressing localization, owing to the incremental forming nature of the process [4], and repeated strain reversals causing loading and unloading relaxations [27]. Incremental sheet forming (ISF) can impart plastic strains well beyond the conventional forming limit curves. Mechanisms facilitating such large strains in ISF are shear stress fields, normal stress (in the thickness direction) fields, bending, and cyclic straining accompanied with local relaxations [28]. A detailed analyses on the effects of shear on stretchability in sheet shaping were presented in [29]. Similarly, analyses of thickness stress on the increased stretchability were presented in [30]. Analyses of cyclic straining boosting the stretchability were performed in [31]. Finally, bending can improve stretchability [2, 32-34]. In particular, the beneficial effect of superimposing bending/unbending on tension to improve stretchability was observed in sheet metal forming with draw-beads [35]. Enhanced stretchability also arises from relaxations [36-38]. The relaxations are reconfigurations of dislocations into their lower energy states [27, 39] relaxing internal backstress fields [40-42]. Low energy cellular dislocation debris in an Al alloy [3] and dislocation tangles in a steel [43]

were observed, owing to the relaxations in repeated loading-unloading in CBT. These dislocation substructures were not observed after simple tension.

The documented benefits of CBT provided the incentive to build a machine aimed at deeper analyses of the effects and mechanisms in the delayed necking achievable by this method. Photographs of the machine are provided in Appendix A. A strip or a sheet of metal is passed back and forth through a stationary roller assembly that imparts bending locally to the strip/sheet, while the strip/sheet is pulled in tension under a constant pulling rate. Plasticity takes place locally during bending. Necking is postponed because ductility is depleted incrementally throughout the gauge length as opposed to localized necking followed by the fracture that is unavoidable in a simple tension (ST) test. At the conclusion of a ST test, the sheet regions outside the necked region have ample residual ductility. In contrast, the CBT process is conceived to exploit such residual ductility, while postponing necking [1]. The benefits of CBT in improving ETF are therefore the greatest in sheet metals that exhibit large necking in ST, such as Al alloys [44] and steels [45]. Only moderate improvements were achieved for alloys like AZ31, because these alloys fail with small necking regions [46, 47]. Similarly, sheet metals with high hardening rates show minimal improvement in CBT [46, 48]. Based upon the ability of CBT processing to delay necking, it was successfully exploited for determining the post-necking hardening behavior of sheets, given that the sheets can be stretched more in CBT than in ST [49-51].

In a recent work, we have achieved improvements several times in ETF using CBT relative to ST for cp-Ti sheets [52]. The material was found suitable for CBT because it exhibits substantial necking and moderate hardening. The present work is concerned with characterizing the behavior of the same material but for sheets of various width, in order to explore ductility levels for strain paths lying between uniaxial tension and plane-strain tension under CBT conditions. To facilitate the study, the CBT machine needed to be upgraded with wide grips to enable the processing of sheets in addition to just narrow strips. The experimental investigation began by testing five sheet widths under previously optimized crosshead velocity and bending depth for the greatest ETF. In order to study the effect of sheet width during CBT, and to better understand the experimental observations from a fundamental viewpoint, process simulations were carried out using the finite element (FE) method in Abaqus. The simulations predicted the load-displacement data and strain fields relying on the strain rate-independent plasticity theory of von Mises (J_2) with isotropic hardening. The simulations were possible because of the successful extrapolation of the flow stress curves for the material. To this end, the established methodology relying on data from CBT processed sheets was used. Specimens were pre-deformed to several strain levels by interrupting the CBT processing, then sub-size specimens were machined from the CBT processed specimens, and finally tested in ST. The measured flow curves from these secondary tests were then shifted for the axial strain accumulated during the pre-deformation to establish the post-necking flow curves of the material. The extrapolated curves were then used to simulate the load vs displacement curves to large number of CBT cycles. Good predictions of the

succession of spikes and plateaus intrinsic to the CBT load vs displacement curves validated the extrapolated flow stress curves. Upon verification, strain fields were probed axially, in width, and through the sheet thickness to infer the influence of specimen width on the achieved ETF in CBT. Measured strain fields using digital image correlation (DIC) verified the predictions. Comprehensive data consisting of many CBT tests and DIC measurements along with simulation results providing insights in the influence of sheet width on ETF in CBT of cp-Ti are presented and discussed in this paper.

2. Material and experimental and simulation procedures

This section introduces the studied material and explains the experimental and simulation procedures.

2.1 Material

1 mm thick sheets of cp-Ti were supplied by Boeing under specification: AMS-T-9046 CP-1 (grade 4) in their annealed condition. Table 1 shows the composition.

Table 1. Chemical composition of 1 mm thick cp-Ti grade 4 (wt.%) sheets.

C	Fe	H	N	O	Ti
0.005	0.19	0.0006	0.004	0.25	Balance

2.2 Simple tension (ST) testing

Monotonic ST tests were performed on an MTS Landmark 370 servo hydraulic testing machine using specimens of 75 mm gauge length and 11.7 mm width to obtain stress-strain curves of the material. A drawing of the specimen is provided in appendix A. The tests were performed at room temperature under a nominal strain rate of 10^{-3} s^{-1} to fracture along the three main sheet directions: rolling direction, RD, diagonal direction, 45°, and transverse direction, TD. Moreover, sub-size specimens of 32 mm gauge length and 6 mm width were tested on the MTS machine to evaluate residual ductility after CBT processing. An MTS extensometer 632.12F-20 and DIC were utilized to measure displacements and strains for each specimen.

2.3 CBT processing

Photographs of the CBT machine are shown in the appendix, while a schematic of the process is depicted in Fig. 1a. Although the machine was designed for processing of sheets, the

works so far have only investigated strips [45, 52]. The present work is the first investigation using wide sheets with the new wide grip fixtures. The maximum width of the wide grips is 240 mm. Details of the machine and the process were presented in our earlier works [53]. Briefly, the machine consists of a moving carriage gripping a specimen between a pair of narrow or wide grips, a pair of load cells at the grips, a hydraulic actuator, a roller assembly, which is stationary and located on the bed, the bed holding a servomotor and a ball screw with the carriage to move it, and the software and hardware for data-collection. The capacity of the load cells is 22.24 kN for the narrow grip setup and 133.5 kN for the wide grip setup, while the hydraulic actuator is rated at 310 kN with a maximum stroke of 305 mm. A program in LabVIEW collects the load cells' axial loads, crosshead speed/velocity, time, and speed of the carriage. The carriage reciprocates with a maximum speed of 66 mm/s, while the applied crosshead speed can take different constant magnitudes. We define a CBT pass as ending after the rollers traverse the gauge length from one side to the other, while a CBT cycle is defined as one forward pass followed by a reverse pass to the original position.

The key CBT process parameters are bending depth and crosshead speed/velocity. A constant crosshead pulling speed is applied at one end of a sheet/strip, while the other end of the sheet/strip is fixed. Rollers impart localized bending/unbending (i.e. plastic deformation/relaxation) by deforming the sheet/strip as the moving carriage forces it through them from one side to the other, while the sheet/strip is also pulled in tension; the gauge length is defined by the extent of travel through the rollers, which increases as the specimen elongates. The stress/strain state caused by an alternating combination of bending/unbending and tension in CBT induces a non-symmetric tension/compression stress/strain profile that alternates the position of the neutral axis cyclically towards the surfaces of the sheet/strip. The compressive region is temporarily stabilized, while the tensile region experiences peak loading, plastically deforming the sheet/strip in this region. The rollers impart incremental plastic deformation region-by-region of the sheet/strip specimen as the rollers induce a moving region of peak tension. The deforming region that moves axially with the rollers experiences a combination of plastic tension and bending, while the rest of the sheet/strip is under elastic tension. The moving regions of plasticity underneath the rollers facilitate uniform elongation of the entire gauge region of the sheet/strip to very large plastic strains. The ductility is essentially depleted throughout the gauge length as hardening takes place uniformly throughout the sheet/strip gauge length until the small region in contact with the rollers experiences necking localization and fracture. In contrast, ST deformation results in severe necking at a single region followed by fracture. The hardening after exhausting the uniform elongation in ST also occurs locally in a neck because the specimen unloads with plenty of remaining ductility after the onset of necking.

An example 11.7 mm strip specimen is shown in Fig. 1, while the geometries of wide specimens are given in the appendix. The 20 mm wide specimen is not shown but is similar to the 11.7 mm strip (apart from the width). Based on the number of rollers each section of sheet/strip passes during a cycle, three deformation regions arise in CBT. The region of the

sheet/strip closest to the grips undergoes one bend/unbend per pass, and is termed the 1x region; next to it is the 2x region, and finally the central region that undergoes three bends/unbends is the 3x region. The gauge length is the 3x region, initially set to 75 mm; the 2x region experiences smaller deformation, while the 1x experiences even smaller deformation. The initial gauge length of 75 mm is consistent with the gauge length of the ST specimens for a fair comparison of ETF. Fig. 1 also depicts a sub-size specimen embedded in the strip with a gauge length of 32 mm and width of 6 mm as per ASTM E8 [54]. These specimens are used for secondary ST testing of strips pre-deformed in CBT to a certain number of cycles. The secondary ST testing was used to obtain flow stress curves for flow stress extrapolation. All specimens used in the study were cut by water jet cutting with slightly oversized dimensions and then were machined to the specified geometry.

2.4 DIC analysis

Digital image correlation (DIC) was used to measure axial, width (i.e. transverse), and through-thickness strain fields. The fields were compared with simulations to enable better understanding of the CBT process mechanics. A speckle pattern was applied to surfaces of interest. To this end, sheets were painted with a Rust-Oleum® high heat spray paint, with white paint being used as the base and black paint being used for the speckle pattern. Finally, Krylon® matte finish spray coating was applied to shield the surfaces from damage due to friction and contact with the rollers. A Point Grey GRAS-20S4M-C camera with a Schneider Xenoplan 1.4-17mm lens was utilized to capture high contrast images with 2MP resolution at four images per second. For axial and width strains, the camera was mounted on a frame attached to the carriage and positioned above the specimen’s surfaces and roller assembly at a fixed height, such that its optical axis was perpendicular to the middle of the area of interest. The camera's focus was between the grip attached to a hydraulic cylinder and the specimen's gauge section. The entire gauge section was not captured due to the roller's interference.

For measuring the through-thickness strains, the camera was mounted on a tripod on the ground and positioned perpendicular to a specimen's edge and adjusted to focus on the designated area of interest marked on the specimen. This ensured accurate capture of the strain field for analysis. To effectively capture the speckle pattern across the sheet's thickness, which was 1 mm, the camera lens was precisely adjusted to enhance resolution. Consequently, only a small region within the 3x area of the specimen was captured and analyzed. The resolution of the recorded images in this study was 0.044 mm/pix. An image of the initial speckle pattern was used as a reference, while the images after deformation were used to obtain strain fields during the process. VIC-2D DIC software from Correlated Solutions® was used for processing images. The software relied on the subset-based method since it was capable of tracking subsets in situations of large deformations. Images were divided into small subsets and then each subset was compared to its counterpart in the reference images to determine their displacements. Normalized squared differences criterion for pixel matching along with subset size of 19 and step size of 4 were chosen while running the software.

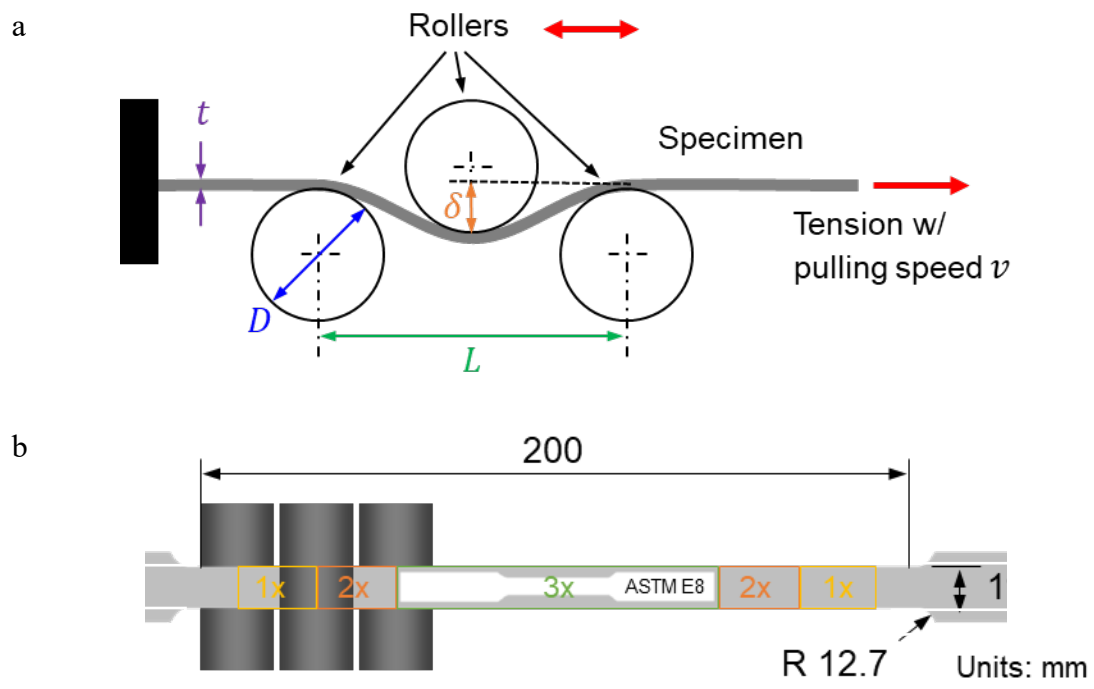

Figure 1: (a) Schematic showing cyclic bending under tension (CBT). Bending depth (δ), set by positioning the top roller, and pulling speed (v) are the main process parameters. Additionally, the distance between the bottom rollers (L) is 54 mm and the diameter of rollers (D) is 25.4 mm. (b) 11.7 mm wide specimen/strip for CBT with indicated 1×, 2×, and 3× deformation regions. Initial length of the 3× region is 75 mm. A sub-size specimen of 6 mm width and 32 mm gauge length for secondary tensile testing is also shown.

2.5 FE simulations of CBT processing

FE models were created in Abaqus to simulate the CBT process. Two of the model setups, along with details pertaining to their meshes, are presented in the appendix. The models are only required to capture one half of the specimens because of longitudinal symmetry. Mesh sensitivity studies were performed for each mesh and mesh biases were quantified to determine the best settings for accuracy and computational efficiency. The rollers were modeled as analytical rigid surfaces. Left ends of the specimens were clamped, while the right ends were pulled with a constant velocity consistent with experiments. The applied speed was 1.35 mm/s, while the top roller was lowered by 3.5 mm, as optimized in the previous study [52]. The coefficient of friction was 0.1 for the hard contact between the rollers and the sheet/strip. The J_2 plasticity theory was used for the simulation. Force and mechanical fields were predicted for comparisons with experiments to facilitate better understanding of the CBT mechanics, as will be presented, and discussed in the next section.

3. Results and discussion

This section presents experimental and simulation results and discusses the findings pertaining to the role of width on ETF of cp-Ti sheets.

3.1 Mechanical response in ST and CBT

Figure 2 shows measured ST engineering and true stress-strain curves of the as-received 1 mm thick cp-Ti sheets. Some plastic anisotropy is observed with TD being the strongest sheet direction, and exhibiting an upper and lower yield point. The rate of hardening in the RD is the highest, approaching the strength of TD at large plastic strains. The 45º direction is slightly softer than TD and RD. The uniform ductility of the material in ST is over 10% in every direction.

Figure 3a shows stress vs displacement curves measured during CBT along RD for cp-Ti sheets of variable width. The optimal bending conditions, which avoid under-bending or over-bending the sheet, established in our prior study for 11.7 mm specimen width, were used in the testing [52]. The curves are given by applied force normalized by the initial area (or engineering stress). The corresponding curve recorded during ST along RD is also shown for reference. The ETF is substantially improved by CBT, compared with ST. The extent of the improvements varies with the sheet width, as shown in Fig. 3b. It should be noted that the axial forces are lower during CBT than during ST since in CBT the deformation is caused by the combination of bending and tension. The ST curve exhibits the typical decreasing work hardening, while the profiles generated in CBT consist of characteristic periodic patterns of spikes and plateaus. The spike regions arise when the rollers are decelerating/accelerating, while the peaks of the spikes indicate stopping of the rollers. The stopping corresponds to pure ST, with no bending except a section of the sheet in bending, but that section is stationary.

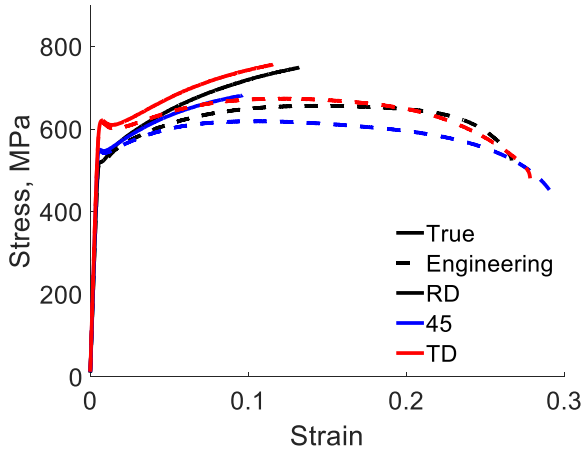

Figure 2: Stress-strain curves measured along the RD, TD, and 45° direction during ST under 0.001/s strain rate at room temperature for as-received 1 mm sheets of cp-Ti (grade 4).

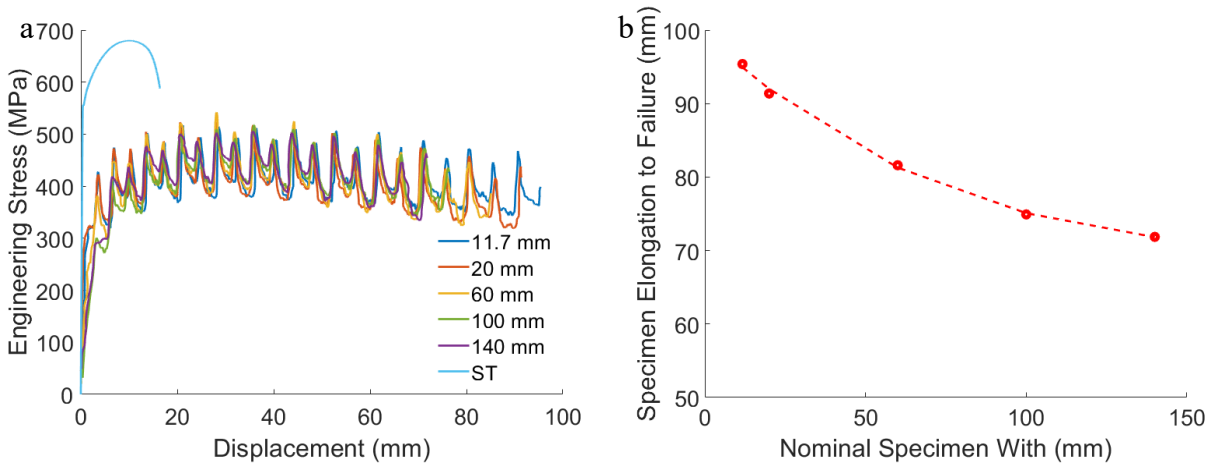

Figure 3: (a) Comparison of measured force normalized by initial area–displacement curves for 1 mm cp-Ti (grade 4) sheet specimens of different width specified in the legend. The CBT testing was performed under 3.5 mm bend depth and 1.35 mm/s pull speed along the RD for all specimens. The engineering stress–displacement curve of the material measured in ST is shown for reference. (b) ETF vs specimen width, along with the dashed trend line.

3.2 Modeling of CBT to extrapolate flow curves and reveal strain fields

The simulations of the CBT process were carried out using the theory of von Mises (J_2 plasticity) [55] requiring true stress-true strain curve and Young's modulus as input material properties. Given some anisotropy in the behavior of cp-Ti, accurate modeling requires more advanced yield criteria [17, 24]. However, the present work models one direction of the sheet at a time (RD, 45˚, TD) for which the von Mises yield criterion is adequate. Owing to the relatively complex kinematics of the CBT process, FE simulations to a large number of CBT cycles are numerically challenging given the very large plastic strains. Nevertheless, 12 CBT cycles were successfully simulated in Abaqus for every width, after proper extrapolation of the flow stress data per the test methods described earlier. .

Figure 4 shows the cp-Ti extrapolated flow curves provided to Abaqus for the simulations of CBT along RD, 45˚, and TD. The curves were extrapolated based on the curves obtained from the secondary ST testing of pre-strained specimens to 2, 6, and 10 CBT cycles. The methodology was established in our prior work [50]. The secondary curves were shifted for the axial strain accumulated during pre-straining. The strain per CBT pass is calculated using a gauge length, l, which is the length that the carriage describes with its velocity, $l = \int v_r dt$, and a specimen elongation from the crosshead motion with its velocity via $dl \approx \Delta l = \int v_c dt$. The

actual integrals were calculated from the experimentally measured profiles as $\Delta\varepsilon = \frac{\Delta l}{l} = \frac{\int v_c dt}{\int v_r dt}$. The accumulated strain after a given number of CBT cycles for the shifts is a sum of the increments per pass (Table 2).

The estimated true-stress vs true-strain curves, based on the secondary tests, were used as initial inputs into the numerical simulations to predict the load vs displacement curves. Some slight adjustments were then made to better fit the data in Fig. 5. The model successfully predicts the succession of spikes and plateaus verifying the extrapolated stress-strain curves for each direction. After successfully reproducing the load vs displacement data for the optimal process parameters, additional data involving two additional bending depths were simulated for further verification. Figure 6 shows these additional comparisons. Note the reduced force levels with the increase in bending magnitude.

A set of the CBT process simulations along the RD for the sheets of different widths was performed next. These simulations facilitated evaluation of the effects of width on the predicted force normalized by the cross-sectional area vs displacement. The force slightly increases with the width of the sheets, as shown in Fig. 7a. The increase is the greatest for the pure plane strain conditions imposed in a 2D simulation, as shown in Fig. 7b.

Finally, the strains in the three major directions are extracted from the CBT simulations of variable width. The distribution of the axial strain along the symmetry line of the specimens of different widths is presented in Fig. 8. The predicted strains are not appreciably different per specimen width. Regions of the sheets processed by the three rollers have the highest strain, while the regions of the sheets processed by two rollers and one roller show much smaller strains. The development of the axial strains in the 3x regions began as relatively uniform for the first few CBT cycles. Subsequently, the axial strains gradually rise at the transition between 2x and 3x regions. The CBT specimens eventually break at these strain localizations between 2x and 3x regions. Fig. 9 presents strains in the width direction, while Fig. 10 presents the through thickness strains for every width. The thickness strain is predicted to increase at the expense of the width strain with greater sheet width, owing to the increasing plane-strain effects, per the volume constancy relationship for plastic deformation (i.e., $\varepsilon_2 = 0$ for a plane-strain condition, and $\varepsilon_1 + \varepsilon_2 + \varepsilon_3 = 0$). The excess material in the width direction in the wider sheets is preventing / reducing the plastic deformation in the width direction. The increased strain in the thickness direction compensates for it. The increase in the thickness strain is a likely reason for the observed earlier localization and failure that led to a reduced ETF as the sheet width was increased. This observation is consistent with forming limit curves that have been measured experimentally for similar cp-Ti (and other) materials, showing that plane-strain tension produces limit strains that are lower than uniaxial tension [56, 57]. Note that in Figs. 8 and 9 data from both the Top and Bottom average nodal values through the thickness are presented. For most plots, these are consistent. However, for Figs. 9a and b, with the narrowest specimen widths of 11.7 and 20 mm, the Top surface has more minor strain in the width direction than the Bottom surface due to the asymmetry in the rollers, i.e., only one roller interacting with the top surface

while two contact the bottom surface. There are also differences between the Top and Bottom width strains for normalized y coordinate data of > 0.8 near the specimen sides.

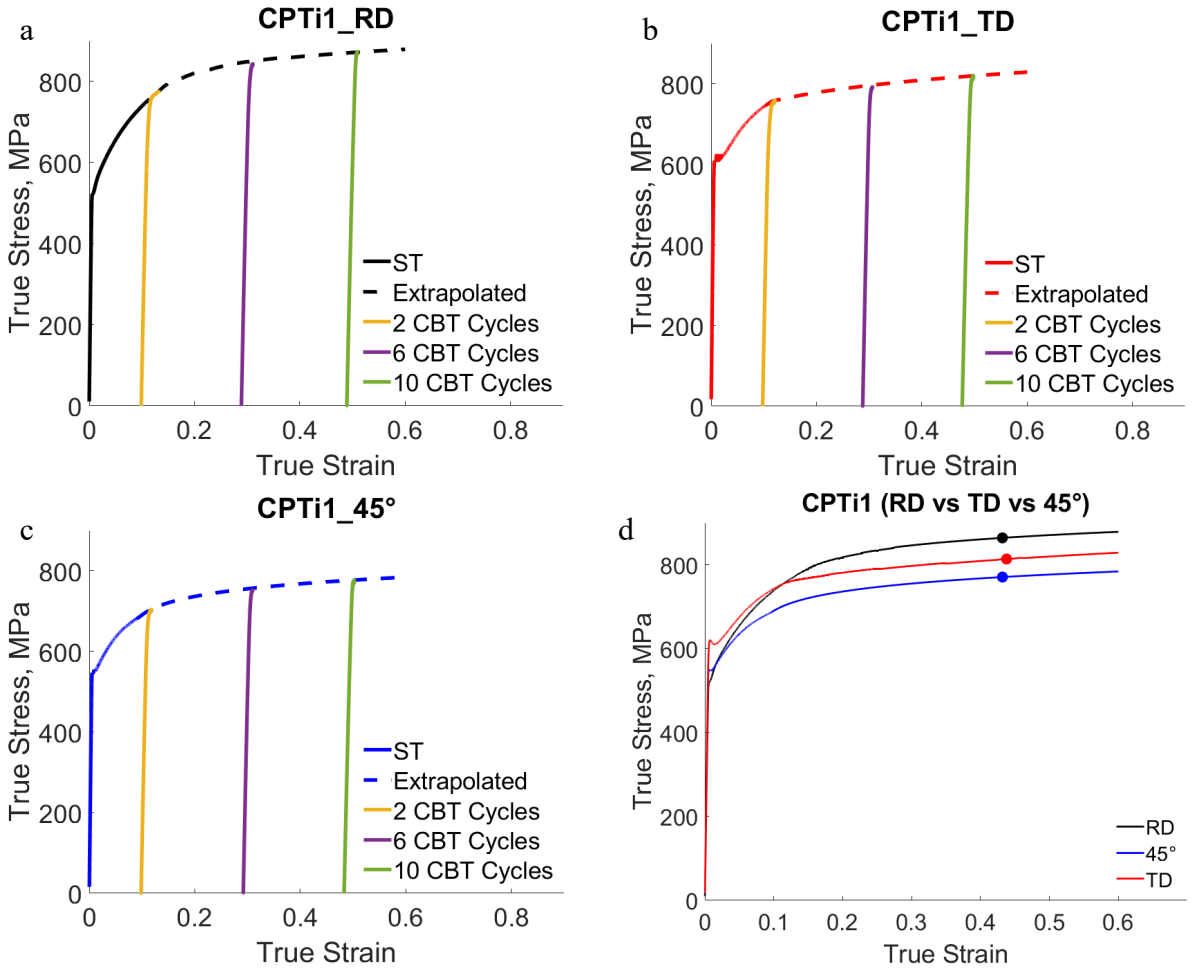

Figure 4: Extrapolated true stress-true strain curves from those in Fig. 2 based on the secondary curves measured from a set of CBT processed sheets to a certain number of CBT cycles indicated in the legends: (a) RD, (b) TD, and (c) 45º. The secondary curves are shifted to the strain levels achieved during the CBT processing. (d) Comparison of the post-necking strain hardening response for the three directions. The points indicate the strain levels at the end of 12 CBT cycles.

Table 2. Strain shifts after a certain number of CBT cycles.

# of cycles	$\mathcal{E}$, RD	$\mathcal{E}$, TD	$\mathcal{E}$, 45°
2	0.099	0.098	0.098
6	0.289	0.288	0.292

10	0.489	0.477	0.483

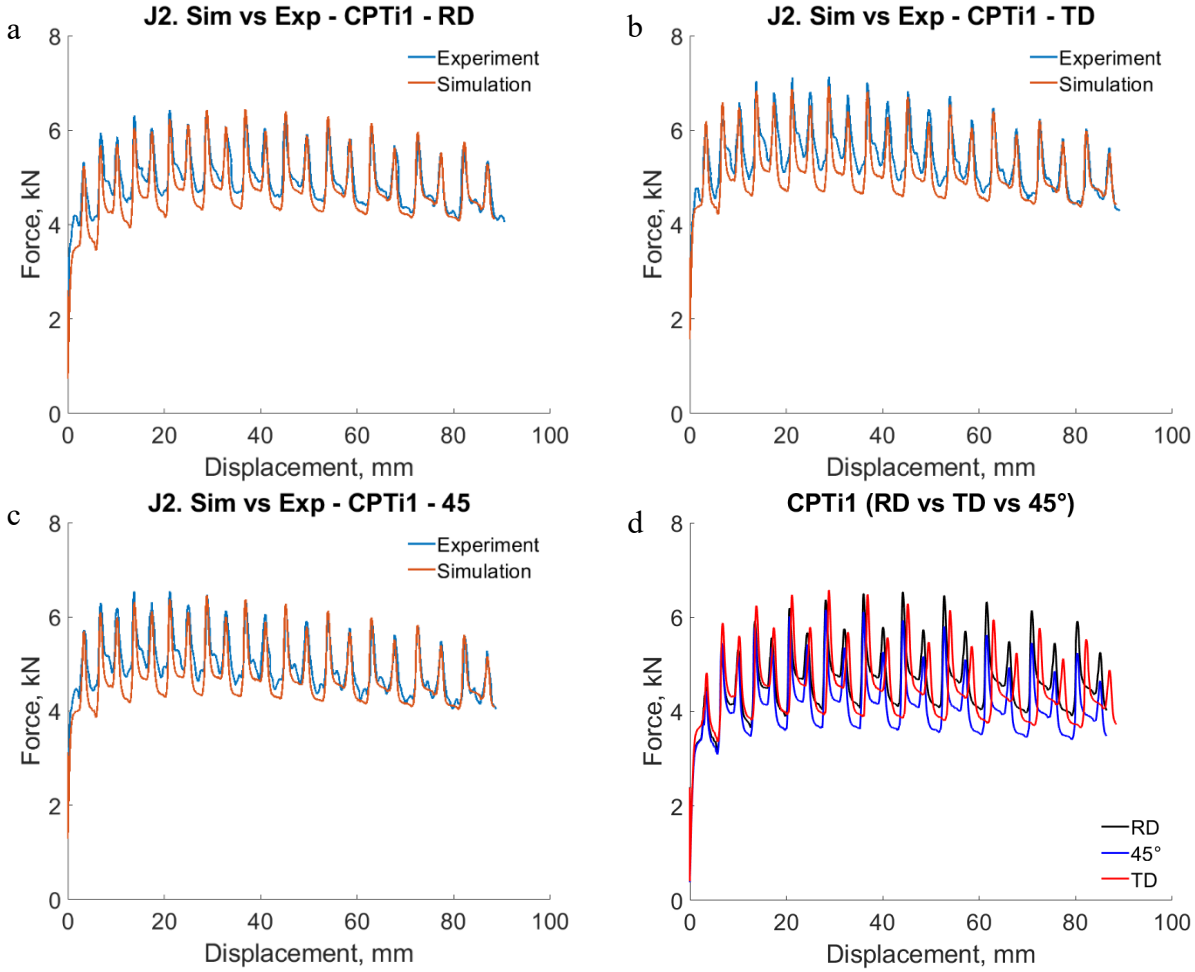

Figure 5: Comparison of measured and simulated force–displacement curves during CBT to 12 cycles including the first cycle under 3.5 mm bend depth and 1.35 mm/s pull speed of 1 mm thick cp-Ti (grade 4) strips of 11.7 mm width used to identify the extrapolated flow curves along: (a) RD, (b) TD, and (c) 45º. (d) Comparison of the three simulated curves.

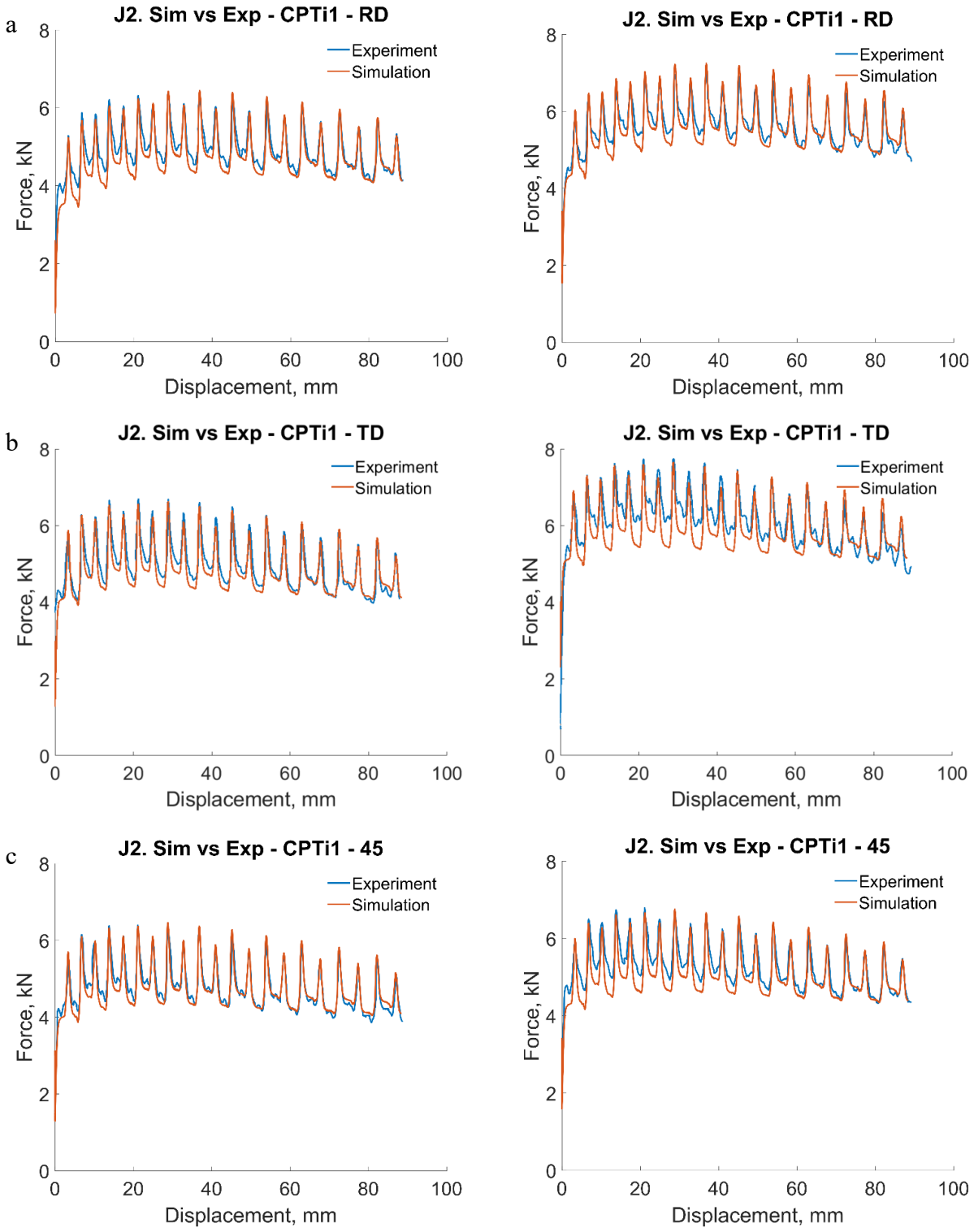

Figure 6: Comparison of measured and simulated force–displacement curves during CBT to 12 cycles under 4 mm bend depth (left) and 3 mm bend depth (right) and the same 1.35 mm/s pull speed of 1 mm thick cp-Ti (grade 4) strips used to verify the extrapolated flow curves along: (a) RD, (b) TD, and (c) 45º.

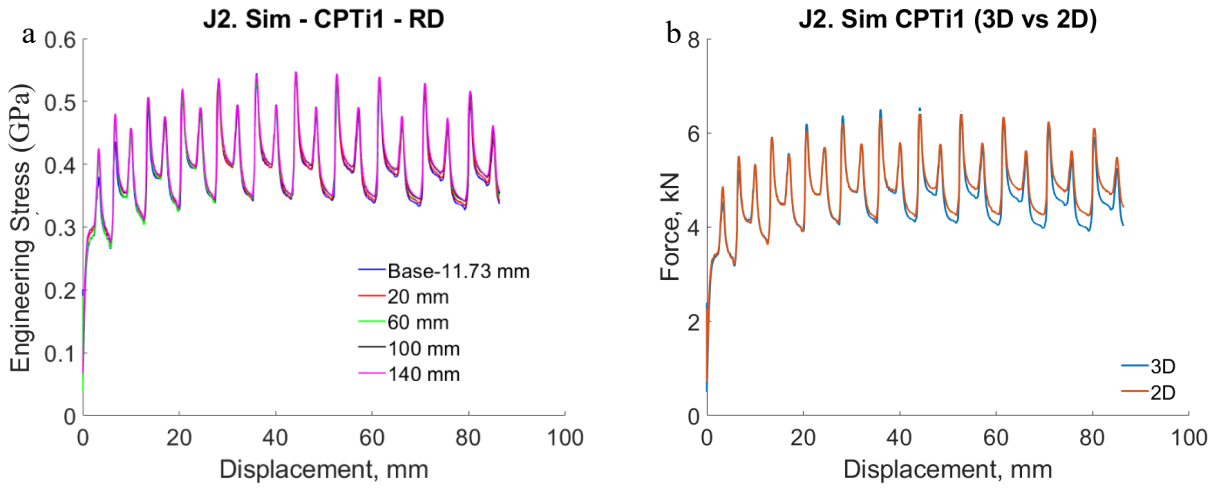

Figure 7: (a) Effect of width on the predicted force normalized by the cross-sectional area versus displacement for 1 mm cp-Ti (grade 4) sheets during CBT along the RD under 1.35 mm/s crosshead velocity and 3.5 bending depth. (b) Comparison of the predicted force versus displacement for 11.7 mm wide sheet simulated in 3D and plane strain conditions simulated in 2D for the same material under the same conditions as in (a).

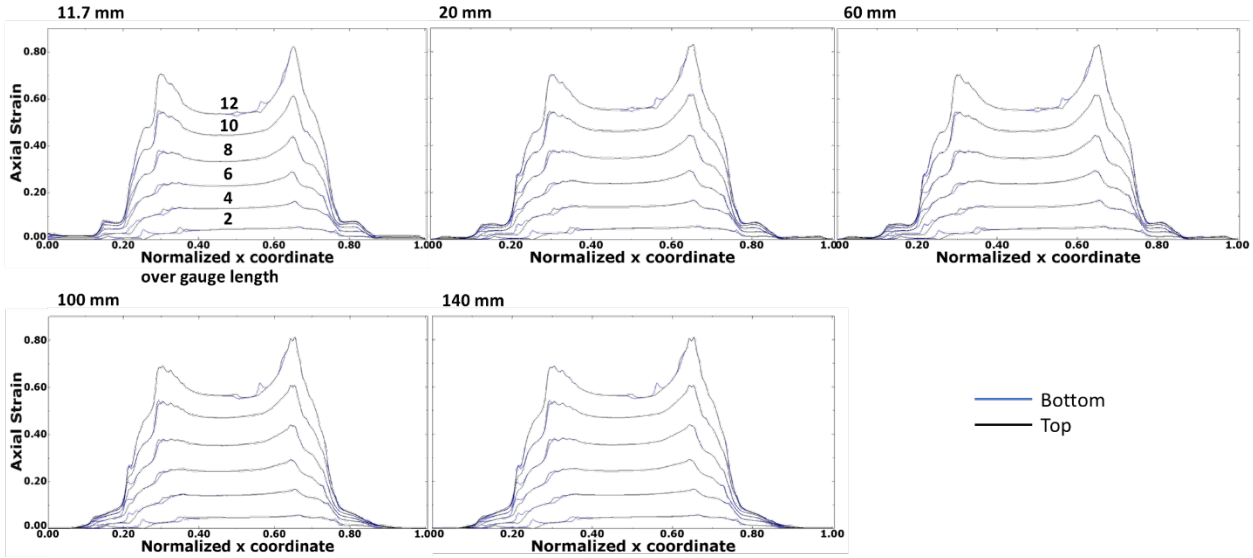

Figure 8: True axial strain recorded at nodes along the gauge section at mid-width symmetry line during CBT simulations under 1.35 mm/s crosshead velocity and 3.5 bending depth along the RD of five specimens having different widths. The numbers in the 11.7 mm plot indicate the number of CBT cycles.

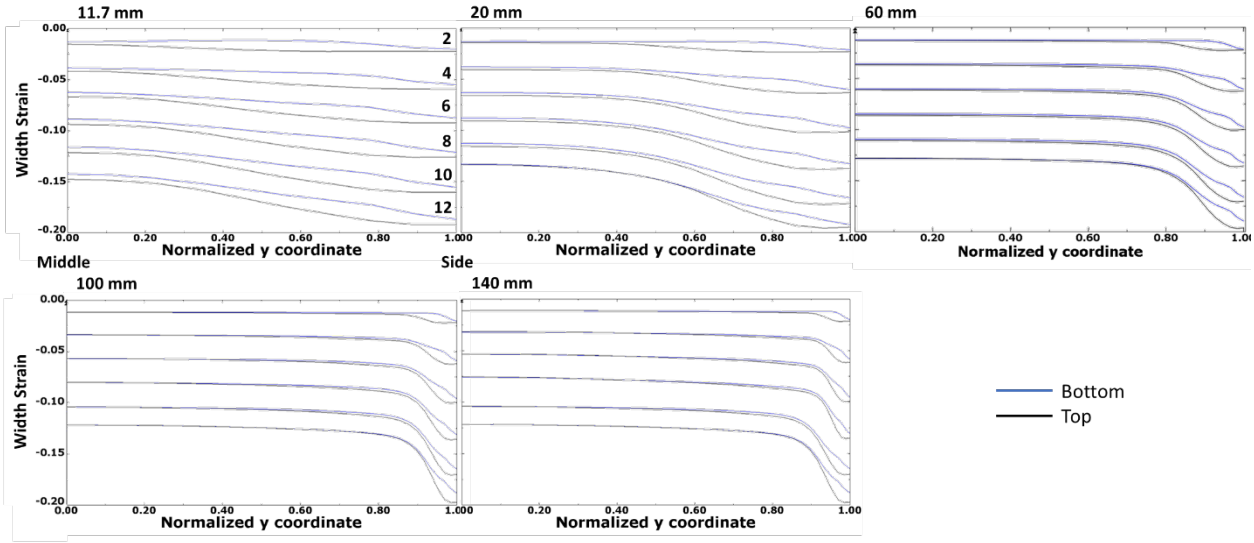

Figure 9: True width strain recorded at nodes along the width at mid-gauge section during CBT simulations under 1.35 mm/s crosshead velocity and 3.5 bending depth along the RD of five specimens having different widths. The numbers in the 11.7 mm plot indicate the number of CBT cycles.

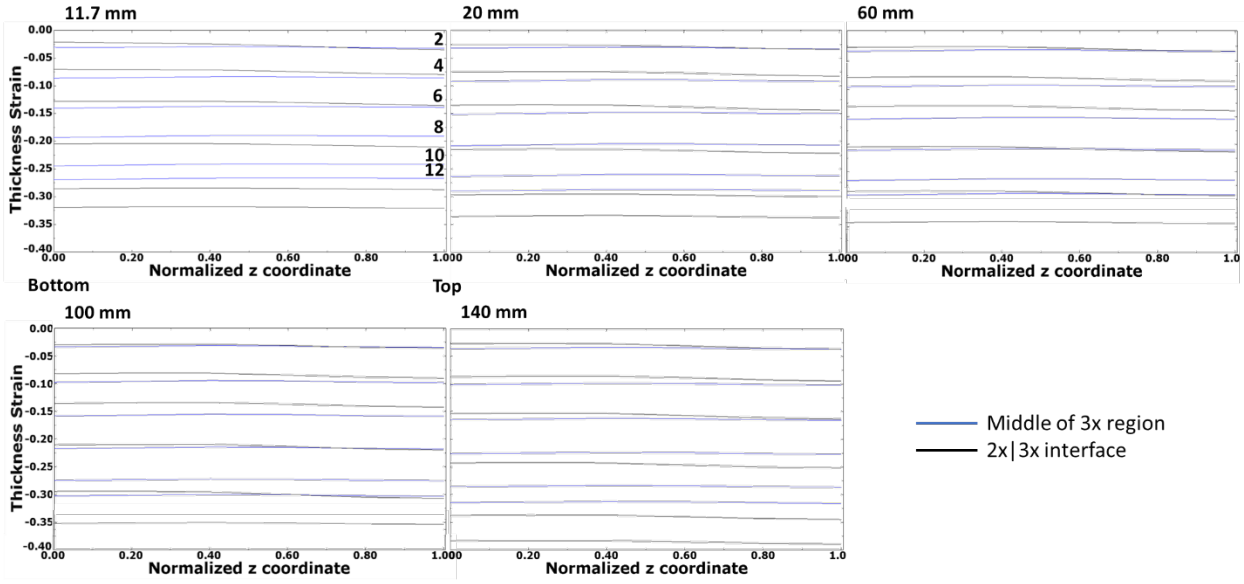

Figure 10: True through-thickness strain recorded at nodes along the thickness at mid-gauge section and at 2X/3X interface during CBT simulations under 1.35 mm/s crosshead velocity and 3.5 bending depth along the RD of five specimens having different widths. The numbers in the 11.7 mm plot indicate the number of CBT cycles.

3.3 Verification of the predictions by comparisons of measured and predicted strain fields

Fig. 11 shows photographs of specimens broken in ST and CBT, along with corresponding undeformed specimens, as references to appreciate the achieved elongations. As can be seen, the CBT process facilitated elongation to greater levels than ST owing primarily to the incremental plastic deformation underneath the rollers. The existence of the stabilizing compressive stress profile and relaxations of the fields are secondary causes of the improved elongation. While the stress profile is intrinsically accounted by the model, the relaxations of the fields require much more advanced models such as those based on the crystal plasticity theories [58]. Quantifying these various effects to clearly demonstrate which one is leading to the increased ETF warrants further investigations using crystal plasticity modeling. Nevertheless, the moving deformation region is modeled properly as the most dominant effect. Moreover, the tensile portion of the stress profile reduced the axial load levels needed for plastic deformation. The FE models show the axial strain contours and deformation regions (1x, 2x, and 3x). Necking is much more pronounced in the specimens tested to fracture in ST than in the specimens tested to fracture in CBT. As the necking begins, any subsequent plastic deformation takes place in the neck, while the rest of the specimen unloads with a lot of capacity to deform plastically; i.e. remaining ductility in the gauge section regions surrounding and away from the neck is substantial. The CBT process better exploits such remaining ductility in ST because CBT suppresses necking. Cp-Ti is a material leaving a substantial amount of remaining ductility after necking; thus, the improvements in ETF using CBT are also substantial. Nevertheless, some necking in CBT is also evident at the 2x/3x interfaces even though the plastic deformation in CBT proceeds to much larger plastic strains than in ST, while depleting the ductility uniformly along the specimen. After the allowable deformation of the material in ST is achieved the material fractures at approximately 45˚ relative to the pulling direction, while the material in CBT quickly localizes and breaks nearly perpendicular to the pulling direction.

Figure 12 compares axial and width strain fields developed during the CBT process based on the number of cycles, as measured by DIC and predicted numerically. The comparison is such that we regard the model to successfully predict the strain fields, as well as the strain localization at the 2x/3x interface. Figure 13 shows measured and simulated strain paths during the CBT process in 3x mid-width region for the different width specimens. It can be seen that the strains are shifting towards plane-strain tension with the specimen width. The experimentally deformed specimens and predictions in Fig. 11 better show the strain localizations and fracture at the 2x/3x interfaces. The fracture occurs in the regions where the rollers moving axially stop restoring pure tension locally and momentarily. Specifically, the region of the sheet underneath the inner roller undergoes the maximum tension corresponding to the peaks in load vs displacement profile and the roller curvature. Such peak loading reduces as the rollers start moving in the opposite direction. Even though the short time duration of the rollers stopping applies some excess plasticity at the 2x/3x interfaces, the developed localizations in CBT at the 2x/3x interfaces are much smaller than necks in ST. The localized regions at the 2x/3x interfaces become the ultimate fracture locations. Figure 14 shows the peak strain fields as similar right before fracture in CBT

of a 11.7 mm wide specimen and the same width ST specimen. The angle of the fracture surface in the CBT specimen was approximately perpendicular to the pulling direction, with small lips near the sheet edges; the ST specimen failure surface had lips that are at approximately 45^{o} to the pulling direction extending about 1/3 of the sheet width from the sheet edges.

The width strain is measured and predicted to be smaller with an increase in the sheet width. Figure 15 shows through-thickness strain fields measured for two sheet widths. The simulation results at the corresponding locations along the sheet are also shown. The results show the trend of increasing the through-thickness strain with increasing sheet width.

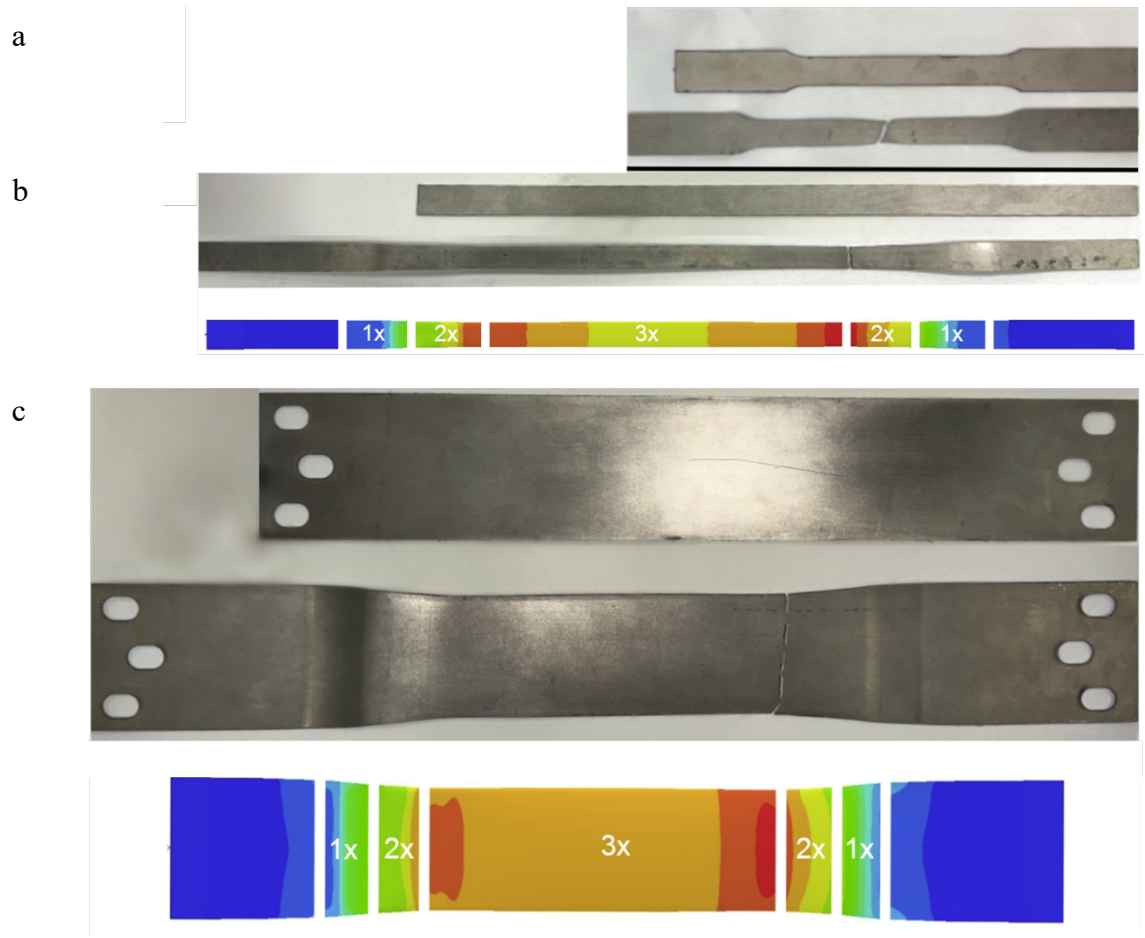

Figure 11: (a) Photographs showing an 11.7 mm wide and 75 mm gauge length undeformed ST specimen and a specimen tested in ST to fracture along RD under 0.001/s strain rate and (b) an 11.7 mm wide undeformed CBT specimen and a specimen tested in CBT to fractured (12.5 CBT cycles) along RD under a bending depth of 3.5 and a pull speed of 1.35 mm/s. At bottom of (b) is a corresponding specimen from the FE simulation showing the axial strain contours. (c) Photographs showing a 60 mm wide undeformed CBT specimen and a specimen tested in CBT to fractured (11.5 CBT cycles) along RD under a bending depth of 3.5 and a pull speed of 1.35 mm/s. At bottom of (c) is a corresponding specimen from the FE simulation showing the axial strain contours.

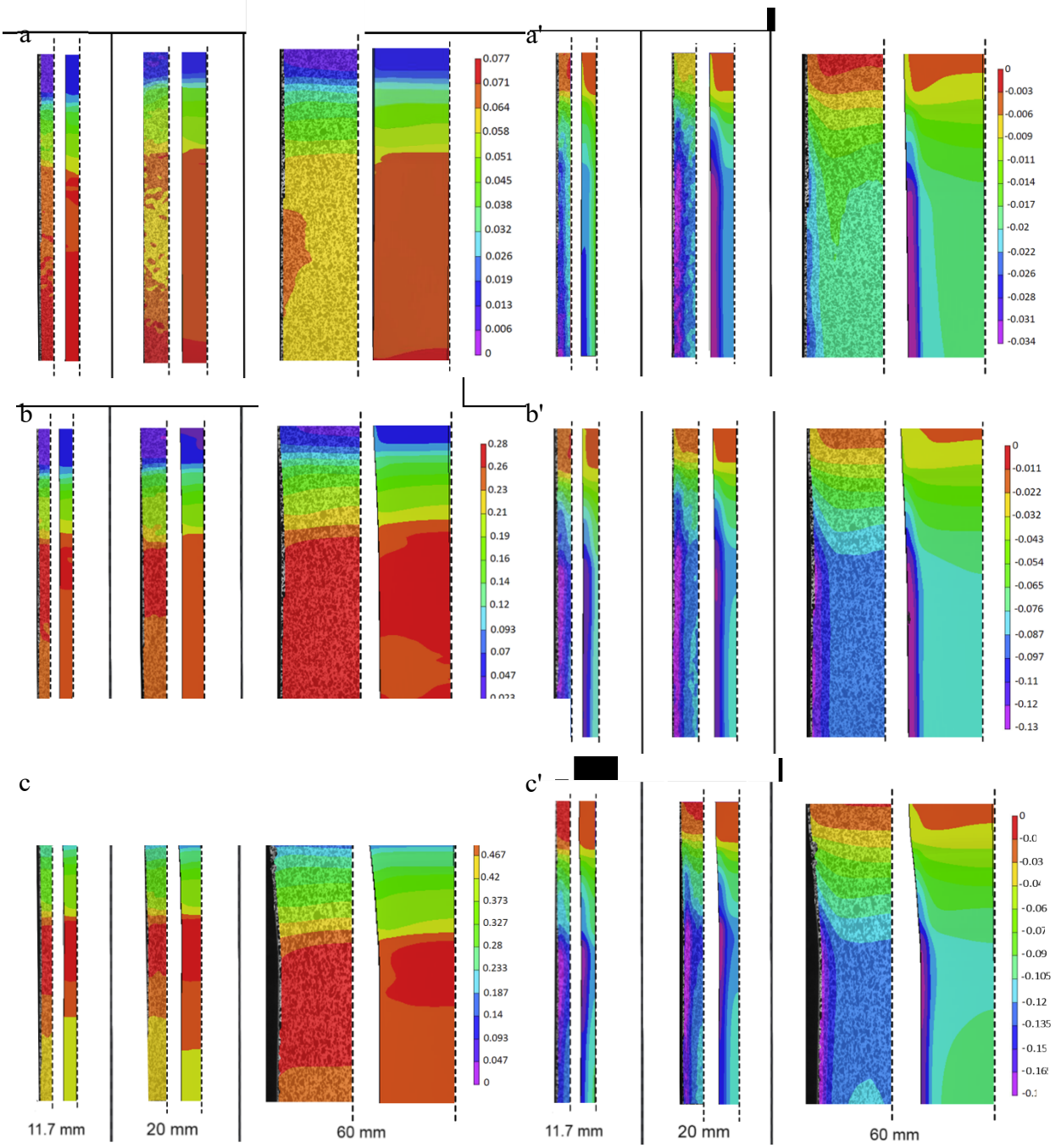

Figure 12: (a, b, c) major (axial) and (a', b', c') minor (width) measured Hencky strain fields (left) and predicted LE strain fields (right) over half-width of specimens after (a, a') 2, (b, b') 6.5, and (c, c') 10.5 CBT cycles for cp-Ti (grade 4) 1 mm thickness sheets of different width, as indicated in the figure. The CBT process parameters of 3.5 mm bend depth and 1.35 mm/s pull speed were used.

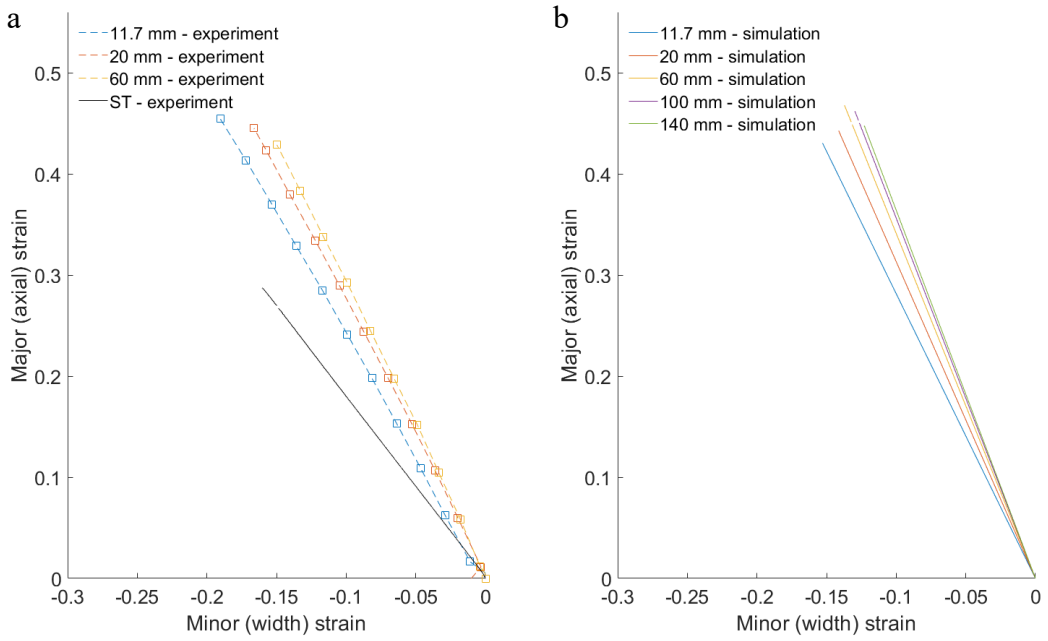

Figure 13: Strain paths during the CBT process in 3x mid-width region for the different width specimens: (a) experiments and (b) simulations. Included is the strain path from simple tension in (a).

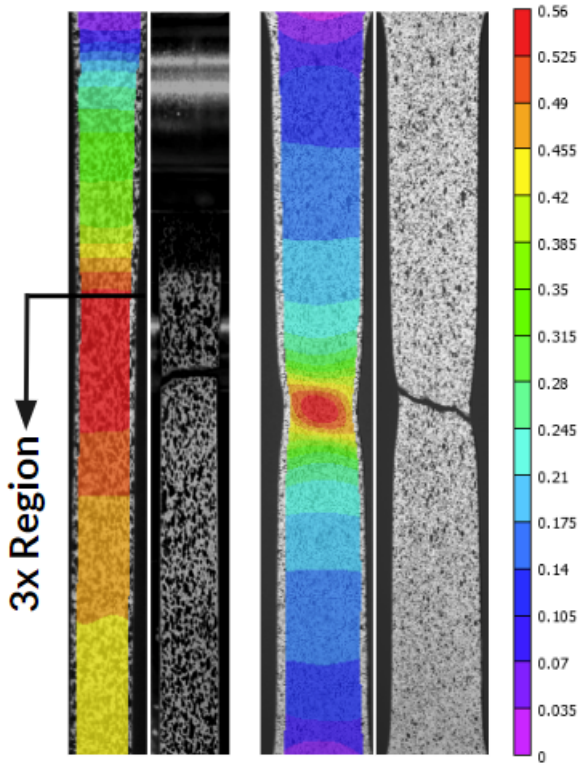

Figure 14: Peak strain fields right before fracture in CBT of a 11.7 mm wide specimen and ST (the same specimen as in Fig. 11).

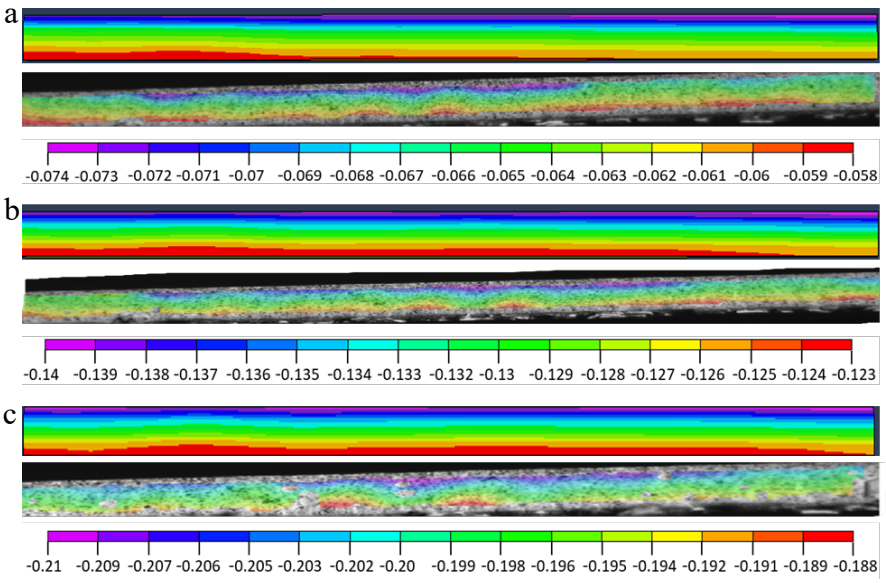

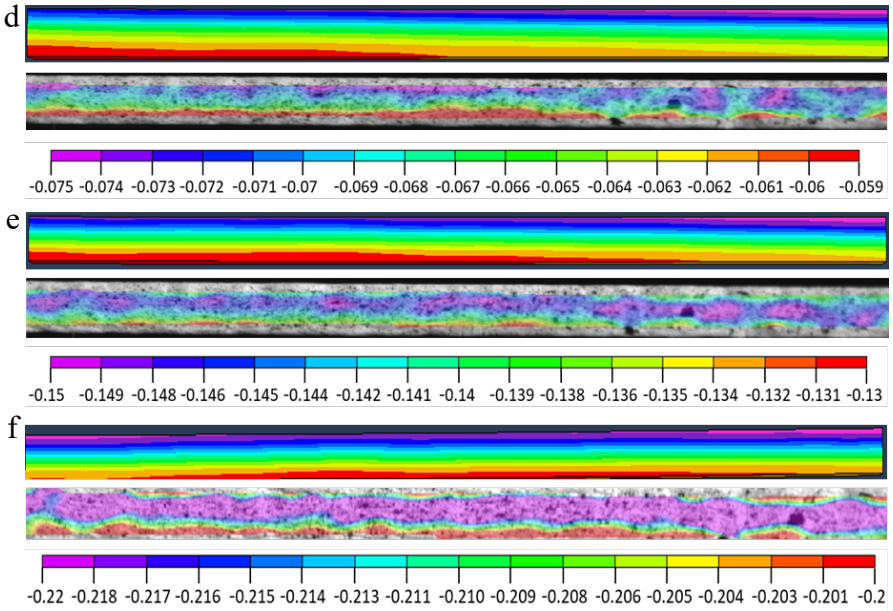

Figure 15: Comparison of measured (bottom) and predicted (top) through-thickness true strain fields after (a, d) 3, (b, e) 6, and (c, f) 8 CBT cycles for cp-Ti (grade 4) 1 mm thickness sheet specimens of (a, b, c) 11.7 width and (d, e, f) 140 mm width. The CBT process parameters of 3.5 mm bend depth and 1.35 mm/s pull speed were used.

In closing, we reflect on the evolution of sheet thickness during CBT and its role during the process. Owing to the combination of bending and tension in CBT, a non-symmetric stress / strain profile is induced with the neutral axis cyclically shifting towards upper and lower sheet/strip surfaces depending on whether the sheet/strip is passing over the upper or lower roller. The tension due to the bending added to the pure tension produces the greatest stress / strain causing the plastic flow locally at the outward edge of the sheet/strip opposite of the touching roller. It is easier to reach the flow stress at the outward edge for a thicker sheet/strip. The edge of the sheet touching the roller is in a state of compression. The compressive portion of the axial stress / strain profile is a welcome stabilization in the CBT process. The sheet/strip during CBT undergoes thinning owing to the strain in the through-thickness direction. The positioning of the neutral axis depends on the current sheet thickness. While it can completely exit the sheet with subsequent thinning, the further it is positioned inside the sheet the better it is for achieving greater ETF. If the neutral axis leaves the interior of the specimen, the entire specimen cross section is constantly in tension, thus accelerating the exhaustion of the remaining hardening and ductility to fracture. Table 3 shows thicknesses of the CBT specimens at fracture. Interestingly, the post-fracture reduction in thickness near the fracture surface is similar for all, even though there is a reduction in the number of cycles to failure with width. Thickness strain is therefore similar at fracture for all specimens, but localization is promoted earlier for wider specimens, by forcing greater thickness strain via constraint on width strain.

Table 3. Measured specimen thicknesses at fracture after CBT. Averages were obtained from several random measurements across the thickness per specimen. Note that the first cycle (without pulling) is counted in the second row.

Nominal Specimen Width (mm)	11.7	20	60	100	140
Cycles to Failure	12.5	12	11.5	10.5	10
Average Thickness (mm)	0.692	0.709	0.698	0.691	0.705
Reduction in Thickness (%)	30.8	29.1	30.2	30.9	29.5

4. Summary and conclusions

The present paper is the first report examining the influence of specimen width on ETF in CBT. The sheet metal used in the study was cp-Ti. The CBT machine was appropriately upgraded with wide grips to enable the processing of wide sheets in addition to narrow strips. A number of FE process simulations were successfully carried out in Abaqus to predict the load vs displacement data and strain fields with the aim of explaining the observations. Since the strain levels during CBT went beyond those possible to achieve during ST, the ST curves per sheet direction were successfully extrapolated. The predictions were verified with corresponding measurements. Comprehensive data consisting of many CBT tests and DIC measurements along with simulation results allowed us to draw the following main conclusions:

- CBT improved ETF of cp-Ti sheets relative to ST for all specimen widths. The primary origin of the improved ETF during CBT is in the separation of a specimen volume into incrementally deforming and moving localized regions underneath the rollers from the rest of the elastically deforming specimen. The existence of the stabilizing compressive stress profile and relaxations of the fields are secondary causes of the improved elongation.
- ETF in CBT reduced as the specimen width of cp-Ti sheets increased and moved closer to plane-strain conditions. The angle of the fracture surface in the CBT specimen was approximately perpendicular to the pulling direction, while the ST specimen failure surface was at approximately 45^{o} to the pulling direction.
- While predicted axial strains were similar for every width, the strain path shifted from uniaxial tension for the narrow specimen toward plane-strain tension for the wider specimens. As such, as plane-strain tension was approached via progressively wider specimens, the width strain was reduced, while the thinning strains increased. Therefore, the increase in the thinning strain is considered the primary reason for the reduced ETF

with increasing sheet width, which is consistent with forming limit curves for this material. The reduction in thickness post-fracture was similar for every specimen width, even though there is a reduction in the number of cycles to failure with width.

Acknowledgments

This work is based upon a project supported by the U.S. National Science Foundation under a GOALI grant CMMI - 2147122 (UNH) and - 2147126 (BYU).

Appendix A

This appendix presents photographs of the CBT tester (Fig. A1), dimensions of the specimens (Fig. A2), and examples of the FE models built in Abaqus to simulate CBT tests (Fig. A3) along with a table specifying the number of elements per FE model (Table A1).

a

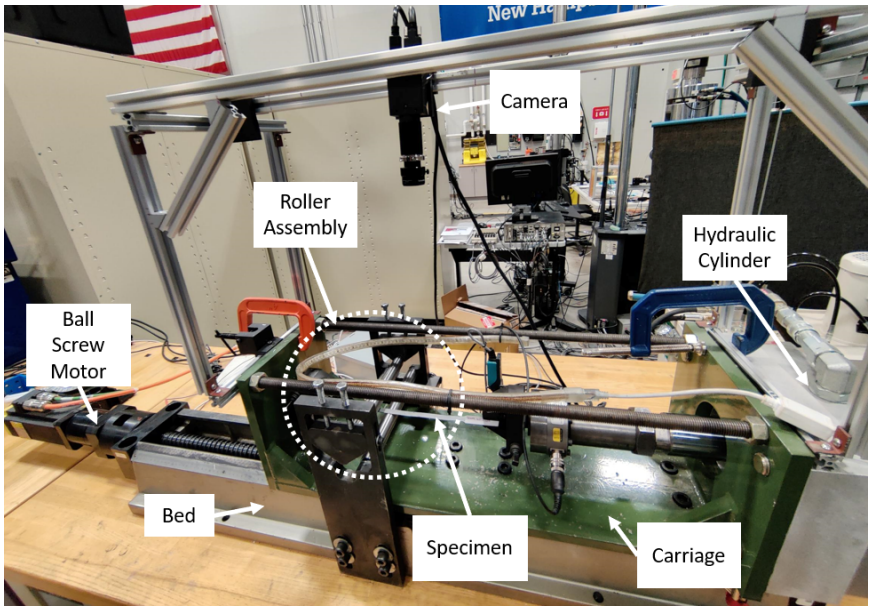

b

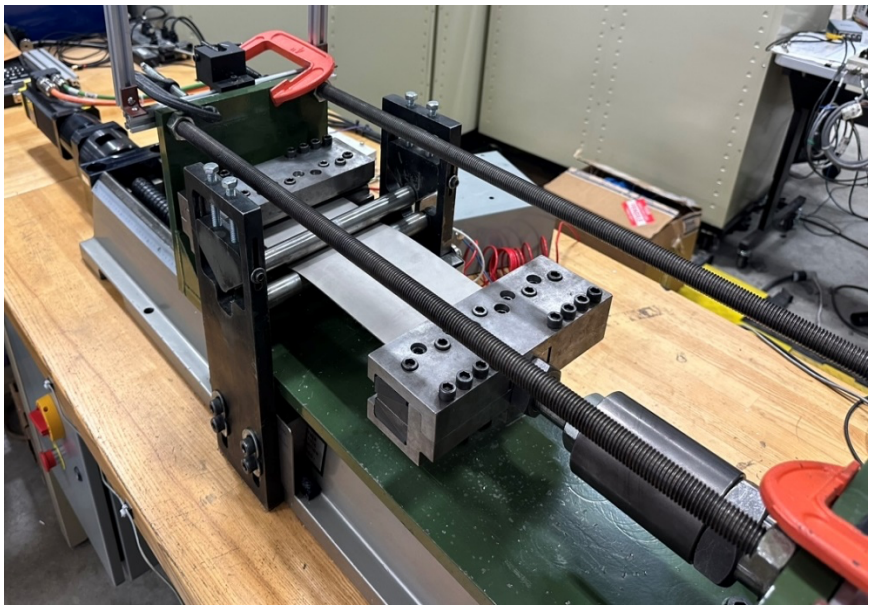

Figure A1. Photograph of the CBT tester: (a) 11.7 mm specimen mounted in regular grips with the main components of the machine identified in the photograph and (b) 140 mm specimen mounted in wide grips.

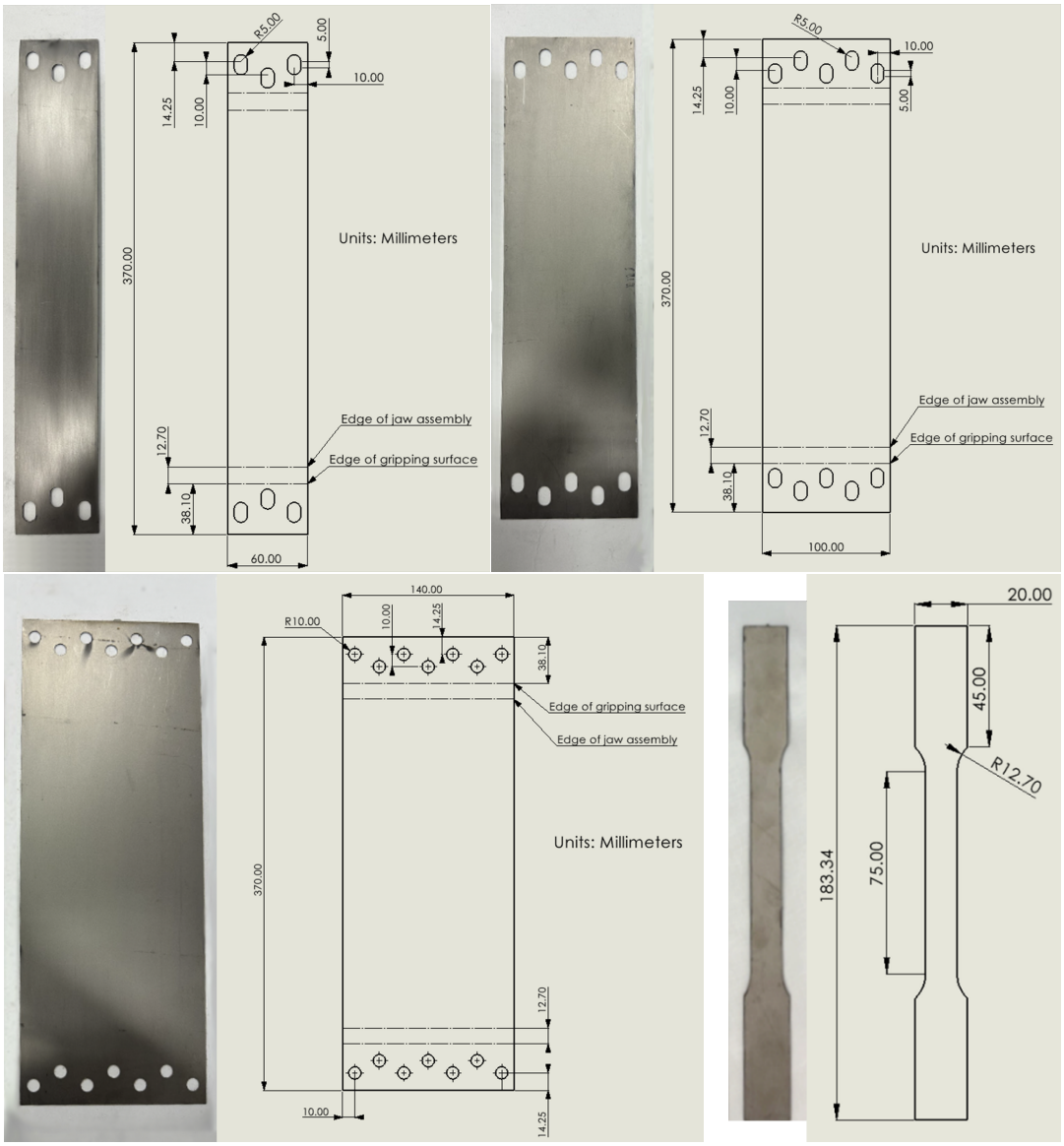

Figure A2. Photographs and drawings of the 60 mm, 100 mm, and 140 mm specimens for the wide grips. 11.7 mm and 20 mm wide strips were 310 mm long for the regular grips. Also, a photograph and a drawing of a ST specimen is provided.

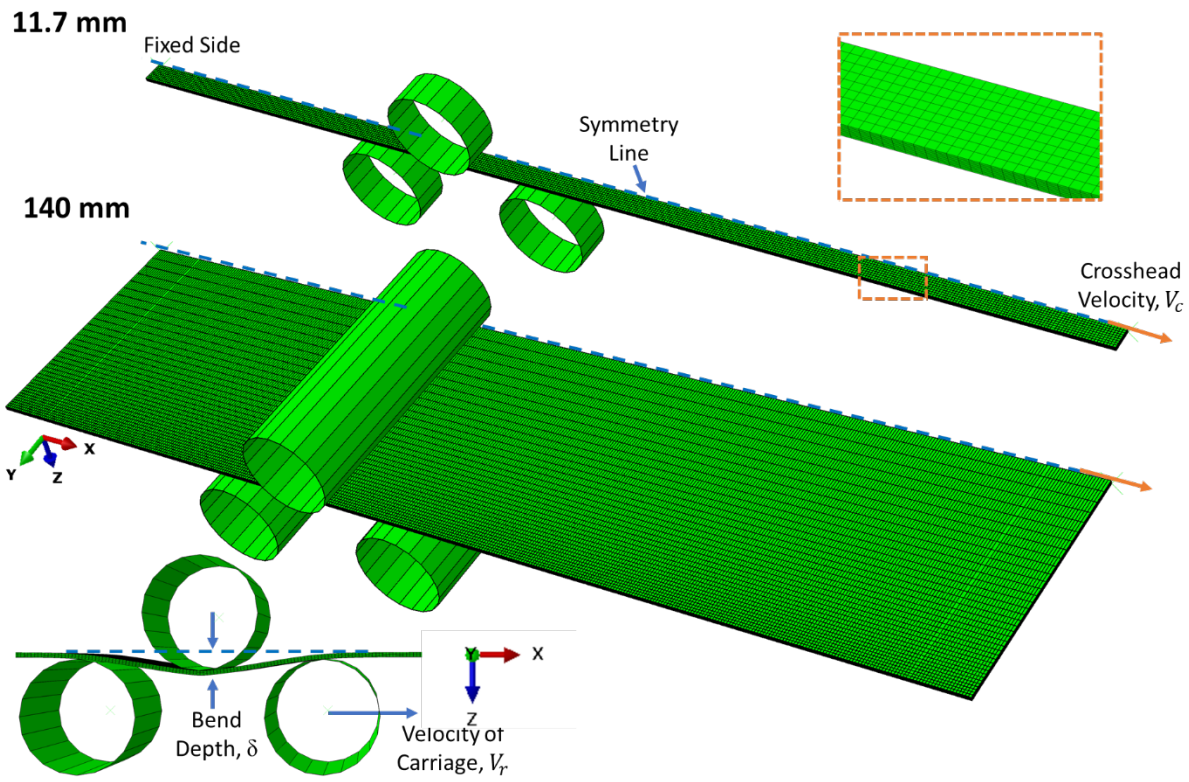

Figure A3. FE meshes for one half of the 11.7 mm and 140 mm specimens consisting of C3D8R elements along with the boundary conditions constructed in Abaqus for simulating CBT. The meshes were 300 mm long. The frame implies x = RD, y = TD, and z = ND. Number of elements per FE mesh are given in Table A1.

Table A1. Number of elements per FE mesh.

Model Width	# of Elements			
	In Thickness	In Half Width	In Length	Total
11.73 mm	5	9	399	17,955
20 mm	5	14	399	27,930
60 mm	5	21	399	41,815
100 mm	5	29	399	57,855
140 mm	5	37	399	73,815

References

[1] W.C. Emmens, A.H. van den Boogaard, Incremental forming by continuous bending under tension—An experimental investigation, Journal of Materials Processing Technology, 209 (2009) 5456-5463.
[2] J. Benedyk, N. Parikh, D. Stawarz, A method for increasing elongation values for ferrous and nonferrous sheet metals, Journal of Materials, 6 (1971) 16-29.
[3] M. Knezevic, C.M. Poulin, X. Zheng, S. Zheng, I.J. Beyerlein, Strengthening of alloy AA6022-T4 by continuous bending under tension, Mater. Sci. Eng. A, 758 (2019) 47-55.
[4] M. Zecevic, M. Knezevic, Origins of improved elongation to fracture in cyclic bending under tension of AA6022-T4 sheets as revealed using crystal plasticity modeling, Mechanics of Materials, 177 (2023) 104546.
[5] M.P. Staiger, A.M. Pietak, J. Huadmai, G. Dias, Magnesium and its alloys as orthopedic biomaterials: a review, Biomaterials, 27 (2006) 1728-1734.
[6] N. Manopulo, C. Raemy, P. Hora, A flexible modelling approach for capturing plastic anisotropy and strength differential effects exhibited by commercially pure titanium, International Journal of Solids and Structures, 151 (2018) 91-98.
[7] J. Zhai, T. Luo, X. Gao, S.M. Graham, M. Baral, Y.P. Korkolis, E. Knudsen, Modeling the ductile damage process in commercially pure titanium, International Journal of Solids and Structures, 91 (2016) 26-45.
[8] J. Wang, M. Zecevic, M. Knezevic, I.J. Beyerlein, Polycrystal plasticity modeling for load reversals in commercially pure titanium, Int. J. Plast., 125 (2020) 294-313.
[9] M. Risse, M. Lentz, C. Fahrenson, W. Reimers, M. Knezevic, I.J. Beyerlein, Elevated Temperature Effects on the Plastic Anisotropy of an Extruded Mg-4 Wt Pct Li Alloy: Experiments and Polycrystal Modeling, Metall. Mater. Trans. A, 48 (2017) 446-458.
[10] M. Zecevic, I.J. Beyerlein, M. Knezevic, Activity of pyramidal I and II <c+a> slip in Mg alloys as revealed by texture development, J. Mech. Phys. Solids, 111 (2018) 290-307.
[11] J. Wang, G. Zhu, L. Wang, E. Vasilev, J.-S. Park, G. Sha, X. Zeng, M. Knezevic, Origins of high ductility exhibited by an extruded magnesium alloy Mg-1.8Zn-0.2Ca: Experiments and crystal plasticity modeling, Journal of Materials Science & Technology, 84 (2021) 27-42.
[12] M. Kaur, K. Singh, Review on titanium and titanium based alloys as biomaterials for orthopaedic applications, Materials Science and Engineering: C, 102 (2019) 844-862.
[13] T.T. Ikuhiro Inagaki, Yoshihisa Shirai, Nozomu Ariyasu, Application and Features of Titanium for the Aerospace Industry, in, Nippon Steel and Sumitomo Metal, 2014, pp. 27.
[14] R.R. Boyer, Titanium for aerospace: Rationale and applications, Adv Perform Mater, 2 (1995) 20.
[15] R. Boyer, An overview on the use of titanium in the aerospace industry, Mater. Sci. Eng. A, 213 (1996) 103-114.
[16] T. Furuta, Chapter 4 - Automobile applications of titanium, in: F. Froes, M. Qian, M. Niinomi (Eds.) Titanium for Consumer Applications, Elsevier, 2019, pp. 77-90.
[17] M. Baral, T. Hama, E. Knudsen, Y.P. Korkolis, Plastic deformation of commercially-pure titanium: experiments and modeling, International Journal of Plasticity, 105 (2018) 164-194.
[18] B. Revil-Baudard, O. Cazacu, E. Massoni, Room-temperature plastic behavior and formability of a commercially pure titanium: Mechanical characterization, modeling, and validation, International Journal of Solids and Structures, 228 (2021) 111121.
[19] H. Becker, W. Pantleon, Work-hardening stages and deformation mechanism maps during tensile deformation of commercially pure titanium, Computational materials science, 76 (2013) 52-59.

[20] L.C. Tsao, H.Y. Wu, J.C. Leong, C.J. Fang, Flow stress behavior of commercial pure titanium sheet during warm tensile deformation, Materials & Design, 34 (2012) 179-184.
[21] J. Peng, C.-Y. Zhou, Q. Dai, X.-H. He, An improved constitutive description of tensile behavior for CP-Ti at ambient and intermediate temperatures, Materials & Design, 50 (2013) 968-976.
[22] X.J. Zhu, M.J. Tan, W. Zhou, Enhanced superplasticity in commercially pure titanium alloy, Scripta Materialia, 52 (2005) 651-655.
[23] L. Filice, F. Gagliardi, S. Lazzaro, C. Rocco, FE simulation and experimental considerations on TI alloy superplastic forming for aerospace applications, International Journal of Material Forming, 3 (2010) 41-46.
[24] T. Hama, H. Nagao, A. Kobuki, H. Fujimoto, H. Takuda, Work-hardening and twinning behaviors in a commercially pure titanium sheet under various loading paths, Mater. Sci. Eng. A, 620 (2015) 390-398.
[25] S. Sinha, N.P. Gurao, In situ electron backscatter diffraction study of twinning in commercially pure titanium during tension-compression deformation and annealing, Materials & Design, 116 (2017) 686-693.
[26] T.R. Bieler, M.A. Crimp, Y. Yang, L. Wang, P. Eisenlohr, D.E. Mason, W. Liu, G.E. Ice, Strain heterogeneity and damage nucleation at grain boundaries during monotonic deformation in commercial purity titanium, JOM, 61 (2009) 45-52.
[27] A. Varma, A. Gokhale, J. Jain, K. Hariharan, P. Cizek, M. Barnett, Investigation of stress relaxation mechanisms for ductility improvement in SS316L, Philosophical Magazine, 98 (2018) 165-181.
[28] W.C. Emmens, A.H. van den Boogaard, An overview of stabilizing deformation mechanisms in incremental sheet forming, Journal of Materials Processing Technology, 209 (2009) 3688-3695.
[29] P. Eyckens, A. Van Bael, P. Van Houtte, Marciniak–Kuczynski type modelling of the effect of Through-Thickness Shear on the forming limits of sheet metal, Int. J. Plast., 25 (2009) 2249-2268.
[30] J.M. Allwood, D.R. Shouler, Generalised forming limit diagrams showing increased forming limits with non-planar stress states, Int. J. Plast., 25 (2009) 1207-1230.
[31] T. Yagami, K. Manabe, T. Miyamoto, Ductile fracture behavior of 5052 aluminum alloy sheet under cyclic plastic deformation at room temperature, Journal of Materials Processing Technology, 209 (2009) 1042-1047.
[32] H. Swift, Plastic bending under tension, Engineering, 166 (1948) 333-359.
[33] S. Tamimi, G. Sivaswamy, M.A. Siddiq, S. Rahimi, A. Leacock, P. Blackwell, Mechanical response and microstructure evolution of commercially pure titanium subjected to repetitive bending under tension, Materials & Design, 193 (2020) 108814.
[34] R. Schleich, C. Held, M. Sindel, M. Liewald, Investigation on the effect of curvature and sheet thickness on forming limit prediction for aluminium sheet metal alloys, International Journal of Material Forming, 2 (2009) 411.
[35] H. Nine, Drawbead forces in sheet metal forming, in: Mechanics of Sheet Metal Forming, Springer, Boston, MA, 1978, pp. 179-211.
[36] K. Hariharan, O. Majidi, C. Kim, M. Lee, F. Barlat, Stress relaxation and its effect on tensile deformation of steels, Materials & Design (1980-2015), 52 (2013) 284-288.

[37] M. Zecevic, Y.P. Korkolis, T. Kuwabara, M. Knezevic, Dual-phase steel sheets under cyclic tension–compression to large strains: Experiments and crystal plasticity modeling, J. Mech. Phys. Solids, 96 (2016) 65-87.
[38] S. Daroju, T. Kuwabara, R. Sharma, D.T. Fullwood, M.P. Miles, M. Knezevic, Experimental characterization and crystal plasticity modeling for predicting load reversals in AA6016-T4 and AA7021-T79, Int. J. Plast., 153 (2022) 103292.
[39] S. Daroju, T. Kuwabara, M. Knezevic, Experimental characterization and crystal plasticity modeling of dual-phase steels subjected to strain path reversals, Mechanics of Materials, 168 (2022) 104293.
[40] K. Hariharan, P. Dubey, J. Jain, Time dependent ductility improvement of stainless steel SS 316 using stress relaxation, Mater. Sci. Eng. A, 673 (2016) 250-256.
[41] N.C. Ferreri, Z. Feng, D.J. Savage, D.W. Brown, B. Clausen, T.A. Sisneros, M. Knezevic, In-situ high-energy X-ray diffraction and crystal plasticity modeling to predict the evolution of texture, twinning, lattice strains and strength during loading and reloading of beryllium, International Journal of Plasticity, 150 (2022) 103217.
[42] M. Zecevic, M. Knezevic, Latent hardening within the elasto-plastic self-consistent polycrystal homogenization to enable the prediction of anisotropy of AA6022-T4 sheets, Int. J. Plast., 105 (2018) 141-163.
[43] K. Yaddanapudi, M. Knezevic, S. Mahajan, I.J. Beyerlein, Plasticity and structure evolution of ferrite and martensite in DP 1180 during tension and cyclic bending under tension to large strains, Mater. Sci. Eng. A, 820 (2021) 141536.
[44] T.J. Roemer, T.J. Barrett, M. Knezevic, B.L. Kinsey, Y.P. Korkolis, Experimental study of continuous-bending-under-tension of AA6022-T4, Journal of Materials Processing Technology, 266 (2019) 707-714.
[45] C.M. Poulin, S.C. Vogel, Y.P. Korkolis, B.L. Kinsey, M. Knezevic, Experimental studies into the role of cyclic bending during stretching of dual-phase steel sheets, International Journal of Material Forming, 13 (2020) 393-408.
[46] N. Matukhno, N. Kljestan, S.C. Vogel, M. Knezevic, Cyclic bending under tension of alloy AZ31 sheets: Influence on elongation-to-fracture and strength, Mater. Sci. Eng. A, 857 (2022) 144127.
[47] N. Matukhno, N. Kljestan, S.C. Vogel, M. Knezevic, Improvements in elongation and tradeoffs in strength and ductility of several Mg sheet alloys through cyclic bending under tension and annealing, International Journal of Material Forming, 16 (2023) 52.
[48] W.C. Emmens, A.H.v.d. Boogaard, Cyclic stretch-bending: Mechanics, stability and formability, J. Mater. Proc. Technol., 211 (2011) 1965-1981.
[49] W. Emmens, A.H. van den Boogaard, Material characterization at high strain by adapted tensile tests, Experimental mechanics, 52 (2012) 1195-1209.
[50] T.J. Barrett, M. Knezevic, Modeling material behavior during continuous bending under tension for inferring the post-necking strain hardening response of ductile sheet metals: Application to DP 780 steel, International Journal of Mechanical Sciences, 174 (2020) 105508.
[51] C.M. Poulin, T.J. Barrett, M. Knezevic, Inferring Post-Necking Strain Hardening Behavior of Sheets by a Combination of Continuous Bending Under Tension Testing and Finite Element Modeling, Experimental Mechanics, 60 (2020) 459-473.
[52] N. Matukhno, N. Kljestan, M. Knezevic, Enhancing elongation and trading off strength versus ductility of commercially pure titanium sheets using cyclic bending under tension and annealing, International Journal of Solids and Structures, 276 (2023) 112324.

[53] T.J. Barrett, S. Takagi, N. Islam, T. Kuwabara, T. Hassan, B.L. Kinsey, M. Knezevic, Y.P. Korkolis, Material modeling and simulation of continuous-bending-under-tension of AA6022-T4, Journal of Materials Processing Technology, (2020) 116658.
[54] ASTM E8/E8M-15a, in: Standard Test Methods for Tension Testing of Metallic Materials, ASTM International, West Conshohocken, PA, 2015.
[55] ABAQUS Version 6, Dassault Systèmes, Providence, RI, USA, (2017).
[56] Y.S. Kim, B.H. Lee, S.H. Yang, Prediction of forming limit curve for pure titanium sheet, T Nonferr Metal Soc, 28 (2018) 319-327.
[57] A.N. Chamos, G.N. Labeas, D. Setsika, Tensile Behavior and Formability Evaluation of Titanium-40 Material Based on the Forming Limit Diagram Approach, J Mater Eng Perform, 22 (2013) 2253-2260.
[58] M. Zecevic, M. Knezevic, An implicit formulation of the elasto-plastic self-consistent polycrystal plasticity model and its implementation in implicit finite elements, Mechanics of Materials, 136 (2019) 103065.